

# The Mass Dependence of the Fundamental Metallicity Relation in Observations and Simulations

LAURA CARNEVALE <sup>1,2,3</sup> ALEX M. GARCIA <sup>1,2,4</sup> PAUL TORREY <sup>1,2,4</sup> SARA L. ELLISON <sup>5</sup> SHWETA JAIN <sup>6</sup>  
PEIXIN ZHU <sup>7</sup> KATHRYN GRASHA <sup>8,\*</sup> RYAN L. SANDERS <sup>6</sup> AND LARS HERNQUIST <sup>7</sup>

<sup>1</sup>*Department of Astronomy, University of Virginia, Charlottesville, VA 22904, USA*

<sup>2</sup>*Virginia Institute for Theoretical Astronomy, University of Virginia, Charlottesville, VA 22904, USA*

<sup>3</sup>*Department of Astronomy, Boston University, Boston, MA 02215, USA*

<sup>4</sup>*The NSF-Simons AI Institute for Cosmic Origins, USA*

<sup>5</sup>*Department of Physics & Astronomy, University of Victoria, Finnerty Road, Victoria, British Columbia, V8P 1A1, Canada*

<sup>6</sup>*Department of Physics and Astronomy, University of Kentucky, 505 Rose Street, Lexington, KY 40506, USA*

<sup>7</sup>*Harvard-Smithsonian Center for Astrophysics, 60 Garden Street, Cambridge, MA 02138, USA*

<sup>8</sup>*Research School of Astronomy and Astrophysics, Australian National University, Canberra, ACT 2611, Australia*

## ABSTRACT

We show that the Fundamental Metallicity Relation (FMR) depends systematically on galaxy stellar mass in both cosmological simulations (EAGLE, SIMBA, Illustris, IllustrisTNG) and Sloan Digital Sky Survey (SDSS) observations. Using a quantitative slope measure, we find that the canonical anti-correlation between metallicity offset and specific star formation rate (sSFR) inverts above  $10^{10.5} M_{\odot}$ . This inversion arises from the inclusion of low-sSFR galaxies and is consistent with the impact of active galactic nucleus (AGN) feedback, which both quenches star formation and preferentially expels centrally enriched gas. We confirm that this behavior is robust to changes in galaxy selection and metallicity diagnostic, and persists out to  $z \sim 1$ . These results demonstrate that AGN-driven outflows shape the high-mass end of the FMR, providing a new framework to test models of galaxy quenching and the baryon cycle in simulations and future observations.

*Keywords:* galaxies: abundances — galaxies: evolution

## 1. INTRODUCTION

The chemical enrichment of galaxies provides a direct record of their evolutionary histories. Metals are produced in stellar interiors during nuclear fusion and released into the interstellar medium (ISM) through stellar winds and supernova explosions (Lacey & Fall 1985; Koeppen 1994; Friedli et al. 1994). At the same time, galaxies accrete metal-poor gas from the circumgalactic medium, fueling new star formation while diluting the ISM (Kereš et al. 2005; Dekel & Birnboim 2006; McKee & Ostriker 2007; Kennicutt & Evans 2012). This ongoing “baryon cycle” of gas inflow, star formation, metal production, and outflow links metallicity and the star

formation rate (SFR) in ways that can be quantified with scaling relations.

One of the most widely studied of these scaling relations is the stellar mass gas-phase metallicity relation (MZR), in which higher stellar mass generally correlates with higher gas-phase metallicity (Lequeux et al. 1979; Tremonti et al. 2004), a trend observed out to high redshifts (Savaglio et al. 2005; Zahid et al. 2014; Sanders et al. 2018; Sarkar et al. 2025). An extension of this relation, the Fundamental Metallicity Relation (FMR), connects stellar mass, gas-phase metallicity, and SFR (or gas fraction) via a three-dimensional surface which is thought to be invariant across time (Ellison et al. 2008; Lara-López et al. 2010; Mannucci et al. 2010). In the FMR, galaxies with elevated SFRs tend to have lower metallicities at fixed mass, an anti-correlation explained by simple gas accretion models (e.g., Davé et al. 2011; De Rossi et al. 2015; Torrey et al. 2018), and fur-

Corresponding author: Laura Carnevale  
lcarnev@bu.edu

\* ARC DECRA Fellow

ther supported by correlations with gas content (Bothwell et al. 2013, 2016). While the existence of an anti-correlation between metallicity and SFR (or gas content) has been confirmed across multiple surveys (e.g., Zahid et al. 2014; Sanders et al. 2018; Nakajima et al. 2023; Li et al. 2023; Stephenson et al. 2024; Curti et al. 2024), open questions remain about possible redshift evolution (Nakajima et al. 2023; Garcia et al. 2024a, 2025a; Curti et al. 2024; Pistis et al. 2024) and whether stellar mass and/or SFR are truly the “fundamental” drivers of metallicity (Baker & Maiolino 2023; Ma et al. 2024; Sánchez-Menguiano et al. 2024; Bassini et al. 2024).

Numerical simulations provide an essential tool for disentangling the physical drivers of the FMR. Large-volume cosmological hydrodynamic simulations can sample tens of thousands of galaxies across a broad mass range while self-consistently modeling gas flows, star formation, and feedback. The MZR and FMR have been reproduced in such simulations (e.g., Davé et al. 2011; De Rossi et al. 2015; Segers et al. 2016; Torrey et al. 2018, 2019; Garcia et al. 2024a, 2025a), enabling controlled tests of the impact of feedback physics. Recent work has shown evidence for FMR redshift evolution in multiple models (Garcia et al. 2024a, 2025a) and suggested a possible mass dependence in EAGLE (De Rossi et al. 2017), potentially linked to feedback from active galactic nuclei (AGN) (Segers et al. 2016).

Despite these advances, a systematic, cross-model quantification of the mass dependence of the FMR, tested consistently across simulations and observations, is lacking. Some studies have hinted that the correlation between metallicity offset and SFR seen in the canonical FMR may weaken or even reverse sign at the highest stellar masses (e.g., Yates et al. 2012; De Rossi et al. 2017), but this behavior has not been uniformly characterized across models or compared directly to observational data. It remains unclear whether such an inversion is a robust physical feature, how sensitive it is to galaxy selection methods, and what mechanisms might drive it.

In this paper, we build on the work of Garcia et al. and De Rossi et al. to address these questions by examining the behavior of the stellar mass–gas-phase metallicity–SFR relation in the EAGLE, SIMBA, Illustris, and IllustrisTNG cosmological simulations, as well as in Sloan Digital Sky Survey (SDSS) observational data. For coherence and clarity, we draw a distinction in the rest of this work between the *FMR* as it is generally referred to, and a *residual correlation (with SFR) about the MZR*. Specifically, we use FMR to refer to the *invariant* relation between stellar mass, gas-phase metallicity, and star formation rate. When discussing specifically the re-

lation between those same parameters that varies with mass or redshift, we refer to a residual correlation about the MZR.

The structure of our paper is as follows. In Section 2, we describe the four different simulations we analyze as well as SDSS. We also explain the selection criteria for the galaxies used in our analysis. In Section 3, we go over our results, showing that there is an inversion of the behavior of the metallicity – specific star formation relation as galaxies exceed a stellar mass of  $10^{10.5} M_{\odot}$ . In Section 4, we consider the effects of changing the galaxy selection criteria (§4.1) and the impact of the choice of SDSS metallicity diagnostic (§4.2). We also expand our results to redshifts  $0 < z < 1$  (§4.3). Lastly, we suggest that this inversion is caused by AGN feedback in high-mass galaxies (§4.4). Finally, we summarize our findings in Section 5.

## 2. METHODS

In our analyses, we use data from four different cosmological simulations, Illustris, IllustrisTNG, EAGLE, and SIMBA, as well as observational data from SDSS. The nature of these simulations provides access to a large number of galaxies (i.e.,  $\sim 10^5$ ) across a wide mass range (i.e.  $M_{\star} \sim 10^8 - 10^{12.5} M_{\odot}$ ) which facilitates our study of the FMR. In addition, using four models that are similar in broader aspects (e.g., box size, numerical resolution), but different in others (detailed implementation of physical processes). This enables meaningful comparisons of the resulting relations while also increasing confidence that any result common to all models reflects a genuine physical trend rather than being an artifact of the specific model implementation (see also recent work by Garcia et al. 2024a,b, 2025a,b; Wright et al. 2024; Lagos et al. 2025). In the same vein, the advantage of using SDSS data is that we have access to information from hundreds of thousands of galaxies across the same wide mass range as the simulations — giving us very similar samples to work with. Comparing this to observational data gives us a reference point on which we can benchmark the simulation predictions against observations. In the following section, we describe each of the models and the SDSS dataset, along with the selection criteria used in our analysis.

### 2.1. Simulations

#### 2.1.1. Illustris

The Illustris cosmological simulation suite (Vogelsberger et al. 2014a,b; Genel et al. 2014; Sijacki et al. 2015) is executed with the moving mesh code AREPO (Springel 2010; Pakmor et al. 2011) using the original Illustris galaxy formation model (Vogelsberger

et al. 2013; Torrey et al. 2014). It employs WMAP cosmology (Hinshaw et al. 2013):  $\Omega_\Lambda = 0.73$ ,  $\Omega_m = 0.27$ ,  $\Omega_b = 0.0456$ ,  $H_0 = 70.4$  km/s/Mpc, and  $\sigma_8 = 0.81$ . The simulations are boxes of side length  $75 h^{-1}$  Mpc, achieving a baryon resolution of up to  $\sim 1.26 \times 10^6 M_\odot$ . Illustris uses the Springel & Hernquist (2003) equation of state to model the dense interstellar medium, which allows star formation above a certain gas density threshold while pressurizing the ISM gas against artificial collapse. Stellar feedback is implemented via kinetic galactic winds that are launched from the star forming gas at a rate proportional to the star formation rate. The velocity of the winds is scaled with the dark matter velocity dispersion.

Nine elements are tracked during the simulation: H, He, C, N, O, Ne, Mg, Si, and Fe. Specifically, chemical enrichment from type Ia and II supernovae, as well as enrichment from asymptotic giant branch stars are included, with metal yields taken from Thielemann et al. (2003), Portinari et al. (1998), and Karakas (2010), respectively.

Black holes of mass  $10^5 M_\odot h^{-1}$  are seeded if the galactic halo mass reaches  $5 \times 10^{10} M_\odot h^{-1}$ . The AGN accretion rate is capped at the Eddington limit and the associated feedback is implemented via both a low and a high accretion mode. The low accretion mode, or ‘radio mode’, injects thermal ‘bubbles’ within a radius of 50 kpc of the black hole. The high accretion mode, or ‘quasar mode’, injects thermal energy into the surrounding region. The transition between these two modes is fixed at 5 percent of the Eddington rate.

### 2.1.2. *IllustrisTNG* (TNG)

IllustrisTNG is a successor of the Illustris cosmological simulation (‘TNG’ standing for The Next Generation; Marinacci et al. 2018; Naiman et al. 2018; Nelson et al. 2018; Pillepich et al. 2018a,b; Pillepich et al. 2019; Springel et al. 2018; Nelson et al. 2019a,b). For ease of reference and to prevent confusion with the original Illustris simulations, we will refer to IllustrisTNG simply by ‘TNG’ from here on. TNG’s physical processes have been modified compared to the original Illustris, to obtain a better match to observational results (Weinberger et al. 2017, Springel et al. 2018). For the purposes of this work, we only briefly list a few of the relevant differences between the updated TNG model and that of Illustris; however, we refer the reader to Pillepich et al. (2018b) for a more complete description of differences. The TNG simulations were also carried using the moving Voronoi mesh code AREPO (Springel 2010, Pakmor et al. 2011).

The cosmology ( $\Omega_\Lambda = 0.692$ ,  $\Omega_m = 0.31$ ,  $\Omega_b = 0.0486$ ,  $H_0 = 67.7$  km/s/Mpc,  $\sigma_8 = 0.8159$ ,  $n_s = 0.97$ ) is adapted from the Planck Collaboration XIII data (Planck Collaboration et al. 2016). The model calibration was done using a combination of the stellar mass function, black hole mass vs. stellar mass at  $z = 0$ , cosmic SFR density function, and the hot gas fraction in galaxy clusters at  $z = 0$ . The simulations are carried out in boxes of various side lengths. Here, we analyze data from TNG100-1, which is performed in a volume of side-length  $75 h^{-1}$  Mpc, achieving an initial baryonic resolution of  $1.4 \times 10^6 M_\odot$ , both comparable to the original Illustris simulation (Pillepich et al. 2018b).

TNG keeps track of how the stellar population evolves, including enrichment from type Ia and II supernovae, as well as from the asymptotic giant branch using metal yields tables from Nomoto et al. (1997), Portinari et al. (1998), Kobayashi et al. (2006), Karakas (2010), and Fishlock et al. (2014). In doing so, the same 9 elements as in Illustris (H, He, C, N, O, Ne, Mg, Si, and Fe) are tracked.<sup>1</sup> Star formation occurs when a certain density threshold is reached. TNG uses the same Springel & Hernquist (2003) equation of state as Illustris.

The stellar feedback has both kinetic and thermal components, with 90 percent being injected as momentum and the remaining 10 percent as an increase in temperature. This injection occurs isotropically. The ejected feedback is temporarily decoupled from the hydrodynamic code. It is added back in after 2.5 percent of the Hubble time has elapsed, or when it reaches a cell below a certain density, whichever happens first.

Similar to the base Illustris simulation, if the halo of a galaxy exceeds  $5 \times 10^{10} h^{-1} M_\odot$ , a black hole of mass  $8 \times 10^5 M_\odot h^{-1}$  is seeded. These black holes can become more massive either by merging with other black holes or by accreting mass. While TNG also has a low and a high modes for black hole feedback (Weinberger et al. 2017, 2018), they are notably distinct from the original Illustris model. The transitional threshold from one to the other varies and depends on the mass of the black hole itself. Critically, this black hole mass threshold roughly corresponds to a transition in galaxies with stellar mass of  $\sim 10^{10.5} M_\odot$  (Weinberger et al. 2017). The lower accretion-rate feedback consists of kinetic energy from winds being added to the environment. The higher accretion-rate feedback consists of a deposition of thermal energy around the black hole. In both modes,

<sup>1</sup> TNG also has a tenth ‘other metals’ field which acts as a proxy for the metal species not explicitly tracked.

the energy is injected isotropically. The injecta are not decoupled from the hydrodynamic code.

### 2.1.3. SIMBA

SIMBA (Davé et al. 2019) is the spiritual successor of the MUFASA (Davé et al. 2016) cosmological galaxy formation simulations. It uses the meshless finite mass mode of the GIZMO hydrodynamics code (Hopkins 2015 and 2017). The gravity is resolved based on GADGET-3, which is also used for EAGLE (Springel 2005).

The following cosmological parameters are used:  $\Omega_\Lambda = 0.7$ ,  $\Omega_m = 0.3$ ,  $\Omega_b = 0.048$ ,  $H_0 = 68$  km/s/Mpc,  $\sigma_8 = 0.82$ , and  $n_s = 0.97$  (Planck Collaboration et al. 2016). The simulations are carried out in boxes of side length  $100 h^{-1}$  Mpc, the largest of the four simulations employed; however the baryon mass resolution of  $1.8 \times 10^7 M_\odot$  is coarser than that of the other three simulations by a factor of 10 (Davé et al. 2019). We therefore make slightly different resolution cuts for our galaxies in SIMBA compared to the other three simulation models (which we discuss further in Section 2.1.5).

SIMBA accounts for eleven elements (H, He, C, N, O, Ne, Mg, Si, S, Ca, Fe) in stellar populations. Enrichment is calculated by taking into account stellar evolution (Iwamoto et al. 1999) and type Ia (Nomoto et al. 2006) and II supernovae (Oppenheimer & Davé 2006). The star formation itself takes into account  $H_2$  densities, as guided by the Kennicutt-Schmidt law (Kennicutt 1998), using Krumholz & Gnedin (2011) for its equation of state.

The stellar feedback in SIMBA is modeled using decoupled two-phase winds, with thermal and kinetic components. 30 percent of the injected wind particles are injected as ‘hot’, their temperature depending on the supernova energy and the wind’s kinetic energy. The injected wind is temporarily decoupled from the hydrodynamics code until its velocity relative to its environment is less than half of that environment’s sound speed (Anglés-Alcázar et al. 2017b, Muratov et al. 2015).

A black hole of mass  $10^4 h^{-1} M_\odot$  is seeded when the galaxy halo reaches a mass of  $10^{9.5} M_\odot$  (Davé et al. 2019). SIMBA contains two AGN feedback modes: a kinetic and thermal jet-mode and a kinetic radiative mode. Both modes inject winds into the surrounding space, although the winds of the jet boost have a much larger velocity (the radiative winds can reach velocities up to 1500 km/s, while the jet winds can reach up to 8000 km/s). The jet-mode is present in black holes if they maintain a minimum mass of  $10^{7.5} M_\odot$  and an Eddington ratio of under 0.2. In both modes, the winds are ejected as bipolar to the plane of the black hole. The ejected winds remain decoupled from the hydrodynamic

code for  $10^{-4} t_H(z)$ , traveling for up to 10 kpc. For cold particles, the accretion is limited by torques up to three times the Eddington limit (Hopkins & Quataert 2011, Anglés-Alcázar et al. 2017a); for hot particles, the accretion follows Bondi-Hoyle up to the Eddington limit (Bondi 1952).

### 2.1.4. EAGLE

The EAGLE simulations (Schaye et al. 2015, Crain et al. 2015) are cosmological simulations using a heavily modified version of Gadget-3 (Springel 2005) called ANARCHY (Schaller et al. 2015), which is a version of the N-body Tree-Particle-Mesh smoothed particle hydrodynamics solver, allowing it to calculate both short- and long-range particle interactions.

The cosmology ( $\Omega_\Lambda = 0.693$ ,  $\Omega_m = 0.307$ ,  $\Omega_b = 0.04825$ ,  $H_0 = 67.77$  km/s/Mpc,  $\sigma_8 = 0.8288$ ,  $n_s = 0.9611$ ) has been adapted from the Planck Collaboration XVI (Planck Collaboration et al. 2014). EAGLE is calibrated using observations, including that of the stellar mass to black hole mass relation and SFR observations per Kennicutt (1998). The simulations are carried out in boxes of side length  $67.8 h^{-1}$  Mpc, with a baryonic mass resolution of  $1.8 \times 10^6 M_\odot$  (Schaye et al. 2015).

Across stellar evolution, EAGLE explicitly keeps track of eleven different elements: H, He, C, N, O, Ne, Mg, Si, S, Ca, and Fe (Schaller et al. 2015). Metal yields are taken from Thielemann et al. (2003; asymptotic giant branch), Portinari et al. (1998; type Ia supernovae), and Marigo (2001; type II supernovae). Star formation occurs when a certain density threshold is reached, which in turn depends on the metallicity of the gas (Schaye 2004). The stellar feedback is purely thermal:  $10^{7.5}$  K are injected into the surrounding area, simulating stellar winds, radiation, and type Ia and II supernovae (Dalla Vecchia & Schaye 2012). EAGLE uses Schaye & Dalla Vecchia (2008) for its equation of state.

A black hole of mass  $10^5 h^{-1} M_\odot$  is seeded in the center of a galaxy if the galaxy’s halo exceeds a mass of  $10^{10} h^{-1} M_\odot$ . These black holes can gain mass either by merging with other black holes or by accretion following Bondi-Hoyle (Bondi 1952, Springel et al. 2005, Schaye et al. 2015). Feedback from these black holes is simulated in the form of an isotropic, thermal injection of  $10^{8.5}$  K, chosen to counteract rapid cooling. The feedback rate from the AGN is determined by the accretion rate of the black hole itself. For a more detailed description of AGN feedback in EAGLE, see McAlpine et al. (2017).

For both stellar and black hole feedback, the heated cells are not decoupled from the hydrodynamic code.



This has the effect that mass, metals, energy, and momentum are transmitted locally, to neighboring cells, unlike in the other simulations — with decoupled stellar feedback and (for the most part) black hole feedback — where a wind particle’s mass, metals, and energy end up in more distant gas cells.

### 2.1.5. Galaxy Selection Criteria

The galaxies used in the analysis are selected depending on their stellar mass and star formation rate (SFR). We place an effective resolution cut by requiring all galaxies in our sample have at least  $\sim 10^2$  star particles. From the Illustris, TNG, and EAGLE simulations, this corresponds to galaxies with total stellar masses above roughly  $10^8 M_\odot$ . From the SIMBA simulation, which has a baryonic mass resolution an order of magnitude lower than the other simulations, we select galaxies with stellar masses above  $10^9 M_\odot$ . We further select galaxies only up to a stellar mass of  $10^{12} M_\odot$ . The small number of galaxies at higher masses leads to substantial noise in the definition of the MZR and FMR.

To obtain metallicity values from observations, strong emission lines from star forming regions are needed. Below a certain SFR threshold, the metallicity values can no longer be reliably evaluated. To evenhandedly compare simulations and observations, we place constraints on the SFR of the simulated galaxies. The criteria selecting star-forming galaxies closely follow a number of previous simulation works (e.g., Hemler et al. 2021; Garcia et al. 2023, 2024a, 2025a). We first select galaxies that have a  $\text{SFR} > 0 M_\odot \text{ yr}^{-1}$ . We then bin the remaining galaxies in mass bins of 0.2 dex and calculate the median specific star formation rate (sSFR;  $\text{SFR}/M_*$ ) in each bin. For all of the galaxies below a stellar mass of  $10^{10.2} M_\odot$ , we define a threshold  $-0.5$  dex below the median sSFR and select all galaxies above this threshold. For galaxies with stellar masses above  $10^{10.2} M_\odot$ , we perform a linear fit of the expected sSFR for the midpoint of the mass bin it belongs to and select those with sSFRs no more than 0.5 dex below this line. The fiducial cut-off value of  $-0.5$  dex as well as the cut-off mass threshold of  $10^{10.2} M_\odot$  are adopted from Hemler et al. (2021). Figure 1 shows the specific star formation rate as a function of stellar mass for the four simulations used in this analysis (as well as SDSS) with the median line plotted as a solid red line and the cut off line 0.5 dex below it as a dashed blue line.

In Section 4 we will discuss the effects of varying this threshold by both raising and lowering it (i.e. raising and lowering the dashed blue line). In Section 3, we will use the fiducial value of  $-0.5$  dex.

## 2.2. SDSS

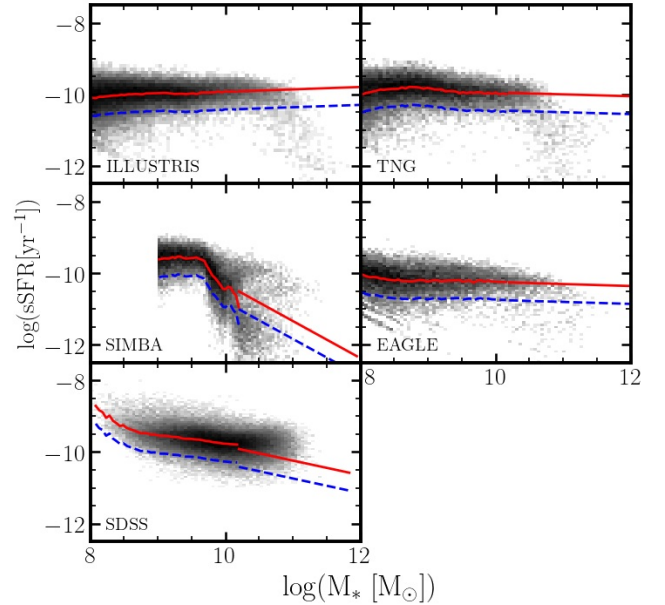


**Figure 1.** Specific star formation rate (sSFR) as a function of stellar mass for Illustris, TNG, SIMBA, and EAGLE simulations and SDSS observations. The median sSFR ( $M < 10^{10.2} M_\odot$ ) and expected sSFR at a given mass ( $M > 10^{10.2} M_\odot$ ) is plotted as a solid red line. The cut-off threshold of 0.5 dex below that is shown as a dashed blue line.

We compare our results from simulations against observationally derived galaxy catalogs from the Sloan Digital Sky Survey (SDSS). Specifically, the observational data for this analysis come from the seventh data release of the SDSS (SDSS DR7) (Abazajian et al. 2009). The release includes spectral analyses of 930,000 galaxies, as well as photometry in u, g, r, i, and z bands. The data was taken using a 2.5m telescope (Gunn et al. 2006) at the Apache Point Observatory in New Mexico. We use stellar mass and SFR values from the MPA/JHU catalog (described, e.g., in Kauffmann et al. 2003; Brinchmann et al. 2004; Salim et al. 2007). For the bulk of this analysis, we use metallicity values ( $12 + \log[\text{O}/\text{H}]$ ) from Curti et al. (2017; using their  $\text{O}_3\text{N}_2$  metallicity diagnostic). In section 4.2, we compare different metallicity diagnostics from DR7 and show that the choice of metallicity diagnostic has virtually no influence on our results. Photometric and astrometric calibrations were done per Hogg et al. (2001) and Pier et al. (2003), respectively.

From the SDSS DR7 data base, we select galaxies that have a signal-to-noise ratio of at least 3 in the 4 emission lines necessary for the BPT diagram (Baldwin et al. 1981). Further, we select galaxies that are classified as star-forming ( $\text{SFR} > 0$ ) per Kauffmann et al. (2003) (selecting galaxies based on where they fall on a plane comparing their  $\text{H}\delta$  emission value to their  $\text{D}(4000)$  value,

which is a means of measuring the break in the optical spectrum at 4000 Å more accurately for young stellar populations).

To match the samples from our simulation datasets, we select galaxies with total stellar masses between  $10^8$  and  $10^{12} M_{\odot}$ . Finally, we filter the observed galaxies in the same way as described for our simulated galaxies (see section 2.1.5), defining a threshold 0.5 dex below the median sSFR and selecting all galaxies that fall above this threshold.

### 3. RESULTS

#### 3.1. Residual Correlation with sSFR about the MZR

##### 3.1.1. Qualitative Comparison of the MZRs

Figure 2 depicts gas metallicity as a function of stellar mass for each of the four simulations (Illustris, TNG, SIMBA, EAGLE) and SDSS at  $z = 0$  on a 2D-histogram. Bins in this relation are colored according to their specific star formation rate (sSFR). In each case, we find an increase in metallicity at higher masses. This is the well-known stellar mass–gas-phase metallicity relation (Tremonti et al. 2004).

In each of the first five panels of Figure 2, the median metallicity is plotted as a red line. The bottom right panel overlays these median metallicity lines, with the one for SDSS plotted as a solid black line and those from the simulations plotted as dashed, colored lines. Comparing these, it is clear that TNG comes the closest in reproducing the SDSS MZR in shape and magnitude, with their median metallicity lines being virtually identical. EAGLE partially reproduces the SDSS result: the median lines have the same overall shape (rising at lower masses and approaching a slope of 0 at higher masses), although EAGLE systematically tends toward higher metallicities. Illustris and SIMBA are unsuccessful in reproducing the observational result. The median MZR for Illustris is much steeper, while that of SIMBA turns up at higher masses, rather than approaching 0. Our finding that TNG is in strong agreement with the observational MZR is notably further in agreement with Jain et al. (2025), who compared the redshift evolution of the MZR in the same four simulations we use to observational results and also find that TNG matches observations the closest.

Within the scatter of the MZR, we find a correlation of the scatter about the MZR with sSFR: at a given mass, galaxies with lower gas metallicities tend to have higher sSFRs, and reversely, galaxies with higher gas metallicities tend to have lower sSFRs. This result in the four simulations is expected based on — and, indeed, identical to (by construction) that of — Garcia et al. 2024a, 2025a. We reproduce the result here for

consistency, showing that it indeed is present in all of the data.

Qualitatively, this residual correlation about the MZR (judged by the color gradient of the MZR graph) agrees well between Illustris, TNG, and EAGLE, with there being a number of high-sSFR ( $\sim 10^{-9.5} \text{yr}^{-1}$ ) galaxies with lower metallicities, and low-sSFR ( $\sim 10^{-10.3} \text{yr}^{-1}$ ) galaxies with higher metallicities. The observational SDSS correlation has the same general trend (higher sSFRs at lower metallicities, and vice-versa), however, its galaxies tend to higher sSFRs overall. There is some correspondence of high sSFR with low metallicity, the highest sSFR galaxies are concentrated at lower masses ( $10^9$  to  $10^{10} M_{\odot}$ ) and the lowest sSFR galaxies are concentrated at higher masses ( $10^{10}$  to  $10^{11.5} M_{\odot}$ ).

##### 3.1.2. Quantitative Comparison of the Scatter about the MZR

We now investigate the behavior of the relation between stellar mass, gas-phase metallicity, and SFR in the simulations and observational data more quantitatively. We obtain the offset of each galaxy’s metallicity from the median MZR (offsets depicted in the inset panels of Figure 2). We fit a linear regression (in logarithmic sSFR) to show the general trend of this relation such that

$$\Delta Z = \eta_{\text{SFR}} \log(\text{sSFR}) + c \quad (1)$$

where  $c$  is constant and  $\eta_{\text{SFR}}$  is the slope. The value of  $\eta_{\text{SFR}}$  gives us a way of quantifying the offsets from the MZR as a function of the sSFR of the galaxy and is related to the commonly used projection of minimum scatter “ $\alpha$ ” value used (see Equation 3 of Garcia et al. 2024a). Thus,  $\eta_{\text{SFR}}$  for all galaxies in the sample gives a baseline for how the FMR acts generally, before we investigate the behavior at different masses more specifically from Section 3.2 onward.

For all five data sources (Illustris, TNG, SIMBA, EAGLE, and SDSS), we find a clear negative relationship, with lower sSFR values correlated with positive values  $\Delta Z$  and higher sSFR values correlated with negative values  $\Delta Z$ . The  $\eta_{\text{SFR}}$  values are as follows:  $-0.17$  for Illustris,  $-0.14$  for TNG,  $-0.16$  for SIMBA,  $-0.26$  for EAGLE, and  $-0.08$  for SDSS. Using  $\eta_{\text{SFR}}$  as a way to measure the FMR, the simulations’ values are all more negative than that from SDSS, with TNG coming closest to the observational value. Importantly, in each simulation and in observations, each of the values of  $\eta_{\text{SFR}}$  are negative, confirming the qualitative trends presented above: the offset from the MZR is anti-correlated with the sSFR of the galaxies.

To conclude the more general discussion of the FMR before moving on to study how it evolves with mass: the

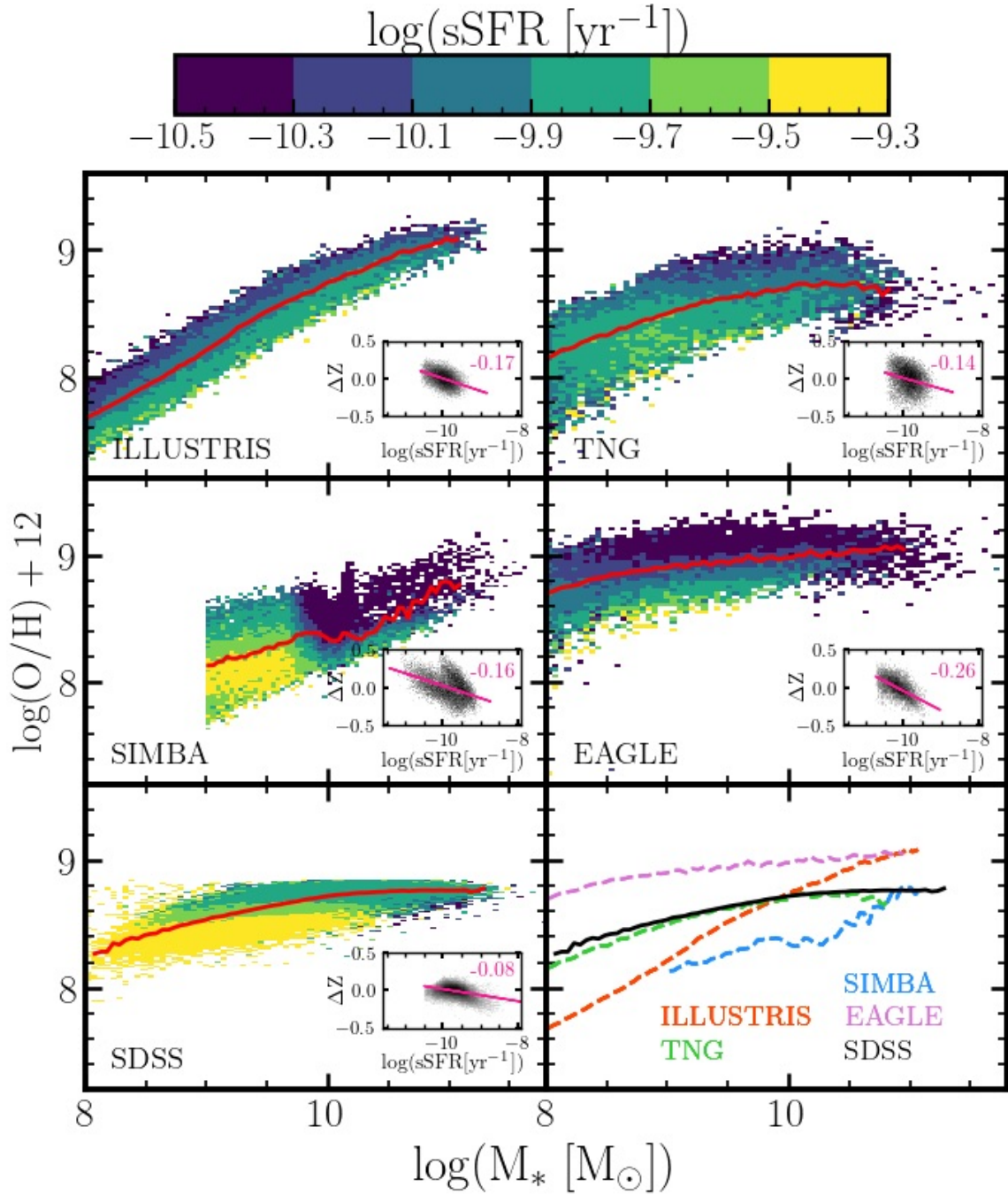


**Figure 2.** Logarithmic graph of stellar mass of a galaxy vs. gas metallicity (mass metallicity relation; MZR) of that galaxy from Illustris, TNG, SIMBA, EAGLE, and SDSS respectively. Color gradient in histogram shows the distribution of specific star formation rate. A line of median metallicity is added. In the corner of each panel is a graph of the galaxies’ gas metallicity offset from the median gas metallicity of its mass bin as a function of sSFR for Illustris, TNG, SIMBA, EAGLE, and SDSS data. A line of best fit is added, with its slope in the upper right corner of each inset. The bottom right panel depicts all five median metallicity lines. The observational SDSS line is plotted solid black, the four simulations are dashed in different colors.

FMR arises in the data we use for our analysis. Further, the relative gas metallicity  $\Delta Z$  and sSFR are generally negatively correlated (negative slope) when considering the global behavior of the FMR at  $z = 0$ .

### 3.2. Stellar Mass Dependence

Next, we investigate how the FMR changes as a function of the stellar mass of a galaxy. To do this, we first sort the galaxies into stellar mass bins of width 0.25 dex.

We then approach the analysis in a similar manner to our analysis in Section 3.1.2: in each of the mass bins, we find the median gas metallicity of the galaxies contained in that mass bin. To quantify this relation, we perform the same linear fit of the data points in each mass bin given by Equation 1.

Figure 3 compares  $\eta_{\text{SFR}}$  values for the four simulations and SDSS as a function of mass. The  $\eta_{\text{SFR}}$  corresponding to each mass bin is plotted at the center of the mass bin, with some slight horizontal staggering for visual clarity. The global average  $\eta_{\text{SFR}}$  value for each data source is superimposed as a horizontal line. We note that  $\eta_{\text{SFR}}$  values are only plotted if at least 50 galaxies are sampled in a particular mass bin. We also perform a bootstrapping analysis as a measure of uncertainty on the derived  $\eta_{\text{SFR}}$  values. Galaxies in each mass bin are randomly sampled (with replacement), from which we then calculate  $\eta_{\text{SFR}}$  with the sample. We perform this bootstrapping 1000 times and quote the median, 16<sup>th</sup>, and 84<sup>th</sup> percentiles in Figure 3. Generally, we find that, at lower masses, the uncertainties in  $\eta_{\text{SFR}}$  are negligible as removing a small fraction of galaxies from the overall sample does not significantly change the overall distribution. However, at higher masses ( $M_{\star} \gtrsim 10^{10} M_{\odot}$ ), the decreased sample sizes mean that random sampling can have a larger effect on the sample. Regardless, we note that none of our key results are significantly impacted by the bootstrapped uncertainty on  $\eta_{\text{SFR}}$ .

For stellar masses between  $10^8$  and  $\sim 10^{9.5} M_{\odot}$ , the  $\eta_{\text{SFR}}$  values are virtually all negative, with a downward (i.e., more negative) trend. This means that lower sSFRs are correlated with higher-than-median metallicities and vice-versa. This behavior is present in the Illustris, TNG, EAGLE, and SDSS data. We note that the lone exception to this is the  $10^8 - 10^{8.5} M_{\odot}$  stellar mass bin in TNG, which has an  $\eta_{\text{SFR}}$  value of  $\sim 0$ . This is likely due to the TNG model having a minimum wind floor, which serves to increase the efficiency of stellar feedback in low mass systems (Pillepich et al. 2018b). We do not have any data points for SIMBA at masses below  $10^9 M_{\odot}$  since SIMBA has ten times poorer resolution than the other three simulations (see Sections 2.1.3 and 2.1.5). However, the  $\eta_{\text{SFR}}$  for the  $< 10^{9.5} M_{\odot}$  SIMBA mass bins are also negative, following the trend of the other four data sources. Between stellar masses of  $\sim 10^{9.5}$  and  $10^{10.5} M_{\odot}$ , the  $\eta_{\text{SFR}}$  values are still negative for all data sources. However, the  $\eta_{\text{SFR}}$  values for TNG, EAGLE, and — to a somewhat lesser degree — SDSS are increasingly less negative with increasing mass bin. For Illustris and SIMBA there is virtually no change, remaining at constant average negative  $\eta_{\text{SFR}}$  values of  $-0.18$  and  $-0.33$ , respectively. At

stellar masses higher than  $\sim 10^{10.5} M_{\odot}$ , we observe an inversion of  $\eta_{\text{SFR}}$  for SDSS, TNG, and EAGLE values, where  $\eta_{\text{SFR}}$  takes on a positive value for the highest mass bin(s). This suggests that, in these highest mass bins, a galaxy’s offset from the MZR is *positively* correlated with its star formation rate: the opposite of the canonical FMR relation. The  $\eta_{\text{SFR}}$  values for Illustris and SIMBA remain negative in this mass range, however.

#### 4. DISCUSSION

In Section 3, we showed that there exists a relation between stellar mass, gas-phase metallicity, and SFR in the data sources we used for our analysis and that this relation shows a stellar mass dependence, inverting at higher masses. In this section, we show that this inversion becomes more prominent across our data sources as we include galaxies with lower sSFRs. We also consider whether the choice of SDSS metallicity diagnostic has an impact on our results and expand our analysis from redshift  $z = 0$  to include redshifts up to  $z = 1$ . Lastly, we suggest a description of the physical mechanism that causes this inversion to happen.

##### 4.1. Changing the Galaxy Selection Criteria Threshold

To investigate the impact of low sSFR galaxies on the value of  $\eta_{\text{SFR}}$ , we change the threshold value for the selection criteria (described in Section 2.1.5). Briefly summarizing, we select galaxies that have a sSFR above a certain value below the median sSFMS. This minimum value is determined by the mass of the galaxy and the threshold value (denoted as ‘T’). The fiducial value of T,  $-0.5$  dex, includes galaxies with sSFRs no more than  $0.5$  dex below the median sSFR values for a given mass bin. In this section, we consider three variations: (i)  $T = -0.1$  dex, (ii)  $T = -1$  dex, and (iii) an effective  $T = -\infty$  dex cut where we consider all systems with  $\text{SFR} > 0 M_{\odot} \text{ yr}^{-1}$ . Reducing the absolute value of this parameter (i.e., changing it to  $-0.1$  dex) will include fewer galaxies, as the threshold is more strict. Conversely, increasing the absolute value of the parameter (changing it to  $-1$  dex or  $-\infty$  dex) will include more galaxies, including those with lower or any non-zero sSFRs.

Figure 4 depicts the equivalent of Figure 3 with the addition of the three changes in threshold value. The top left panel depicts the value of  $\eta_{\text{SFR}}$  as a function of mass for a threshold of  $T = -0.1$  dex. With this highly restrictive sSFR cut, for virtually every mass bin and every data source, we find that  $\eta_{\text{SFR}}$  is negative. There are a few outliers (one low mass bin for SDSS and the highest mass bins for SDSS and EAGLE), but even these slopes are barely greater than zero.

The top right panel is identical to Figure 3, which was previously described in Section 3.2. Both bottom panels



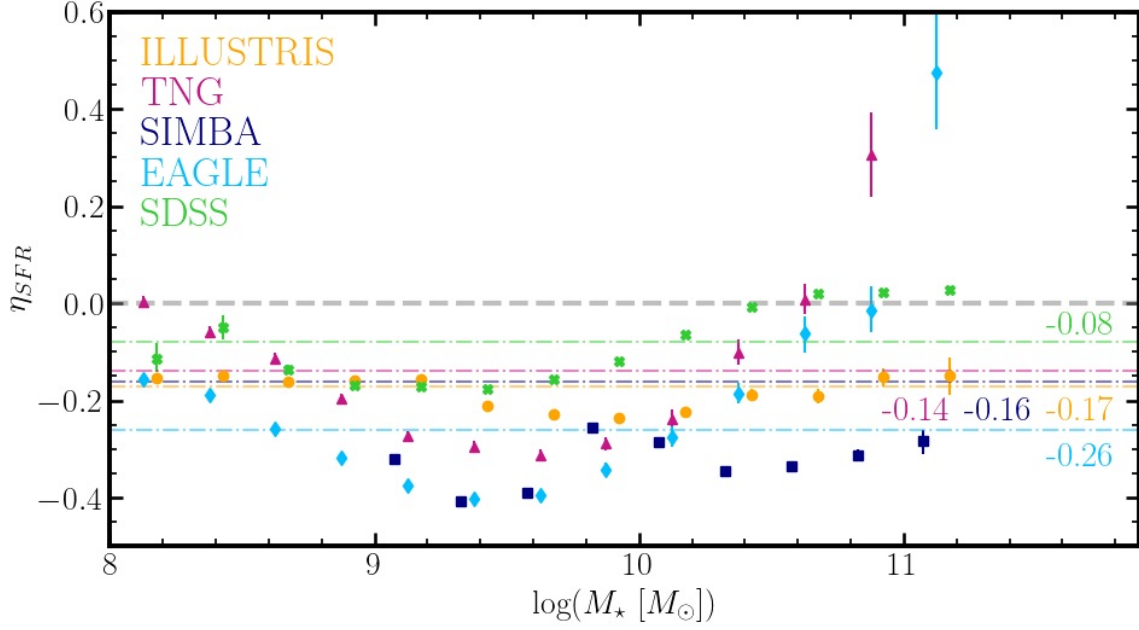


**Figure 3.** Comparison of the trend in offset from median metallicity as a function of sSFR ( $\eta_{\text{SFR}}$ ) for mass bins of width 0.25 dex for each of the four simulations used (TNG, Illustris, SIMBA, EAGLE) and SDSS. Horizontal lines of the global  $\eta_{\text{SFR}}$  value for each data source (from Figure 2), along with that specific value, are superimposed.

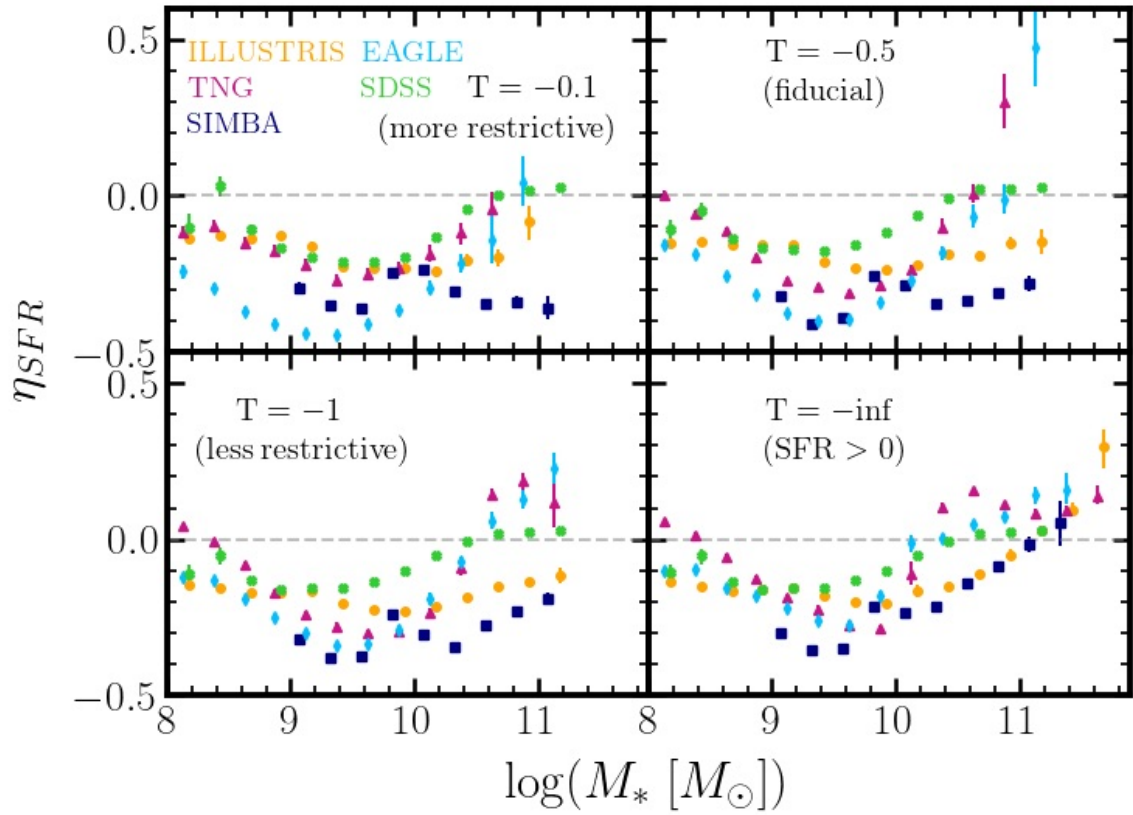


**Figure 4.** Comparison of  $\eta_{\text{SFR}}$  values as a function of mass for mass bins of width 0.25 dex for each of the four simulations (Illustris, TNG, SIMBA, EAGLE) and SDSS with four different sSFR selection threshold values (denoted ‘T’):  $-0.1$  dex (top left),  $-0.5$  dex (fiducial, top right),  $-1$  dex (bottom left), and  $-\infty$  dex (bottom right).

depict  $\eta_{\text{SFR}}$  as a function of mass bin for relaxed selec-

tion criteria (i.e. thresholds that allow low sSFR galax-

ies to be selected). In both panels, we observe a similar pattern as for the top right panel (Figure 3) for SDSS, TNG, and EAGLE: for stellar masses between  $10^8$  and  $10^{9.5}M_\odot$ , the  $\eta_{\text{SFR}}$  values are negative with a negative trend as the mass increases. Then, for stellar masses between  $10^{9.5}$  and  $10^{10.5}M_\odot$ , while  $\eta_{\text{SFR}}$  is still negative, the values are approaching zero as the mass increases. At masses  $> 10^{10.5}M_\odot$ ,  $\eta_{\text{SFR}}$  values for TNG, EAGLE, and SDSS are positive (the same as for  $T = -0.5$  dex). We also note that the lowest mass bins  $\eta_{\text{SFR}}$  value for TNG have a positive slope for  $T = -1, -\infty$  dex. The behavior of Illustris and SIMBA for a threshold of  $T = -1$  dex is the same as for the fiducial threshold, with negative  $\eta_{\text{SFR}}$  values at every mass. Remarkably, however, this changes when using a threshold of  $T = -\infty$  dex: while Illustris and SIMBA still have negative  $\eta_{\text{SFR}}$  values at lower masses, at  $M_\star \gtrsim 10^{11}M_\odot$ , they take on positive values. Therefore using  $T = -\infty$ , we find an inversion of  $\eta_{\text{SFR}}$  at the highest masses for all five data sources.

We suggest that these findings are significant in the following way: when including only high sSFR galaxies ( $T = -0.1$  dex),  $\eta_{\text{SFR}}$  values are negative and we do not see an inversion at higher masses. This result (negative  $\eta_{\text{SFR}}$  values) is also what would be expected based on our mass-independent analysis of the FMR in Section 3.1.2 (Figure 2). We start to see the inversion of  $\eta_{\text{SFR}}$  at higher masses for some of our data sources when we relax the galaxy selection threshold to include some lower sSFR galaxies ( $T = -0.5, -1$  dex). Once we relax this threshold all the way to include all galaxies that have a non-zero sSFR ( $T = -\infty$  dex), we see the inversion of  $\eta_{\text{SFR}}$  at higher masses for all five of our data sources. This suggests that the inversion is related to (and caused by) the presence of these low sSFR galaxies.

#### 4.2. Choice of SDSS Metallicity Diagnostic

While the simulations we use allow us to directly obtain specific values for metallicity, this is not as easily done when calculating metallicity from observations. In our analysis, we use the  $12 + \log[\text{O}/\text{H}]$  values from  $\text{O}_3\text{N}_2$  indices as per Curti et al. (2017). However, the SDSS DR7 also includes many other metallicity estimators, each having some fundamental uncertainty on their own. We recreate our analysis using nine different metallicity diagnostics from six different papers to show that our results arise across all of them. This comparison is depicted in Figure 5. Specifically, the different metallicity diagnostics we use are as follows: *C17O3N2* and *C17N2* describe the Curti et al. (2017) values for the metallicity using  $\text{O}_3\text{N}_2$  and  $\text{N}_2$  indicators, respectively. Similarly, *M13O3N2* and *M13N2* describe the

Marino et al. (2013)  $\text{O}_3\text{N}_2$  and  $\text{N}_2$  indicator metallicity values and *PP04O3N2* and *PP04N2* describe the Pettini & Pagel (2004)  $\text{O}_3\text{N}_2$  and  $\text{N}_2$  indicator metallicity values. *M91*, *KK04*, and *D16* respectively describe the McGaugh (1991), Kobulnicky & Kewley (2004), and Dopita et al. (2016) metallicity values.

The difference between the diagnostics lies in their method of calibration. Each diagnostic generally use strong-line-methods, which entails calibrating the ratio of lines with a known metallicity dependence against the oxygen content of the galaxy. Curti et al. (2017) combine the strong-line-method with the use of electron temperature (anti-correlated with metallicity) and stacking galaxy spectra to empirically obtain metallicity values. Similarly, Marino et al. (2013) combine the strong-line-method and the use of electron temperature in their calibration. Pettini & Pagel (2004) also use the strong-line-method. In the cases of McGaugh (1991), Kobulnicky & Kewley (2004), and Dopita et al. (2016), this calibration was done in a more theoretical way, using photoionization models.

As is clearly visible in Figure 5, all nine diagnostics are in strong agreement. The figure depicts the analysis performed in section 3.2 using galaxy selection threshold  $T = -0.5$ . The galaxies are all selected at  $z = 0$ . For each mass bin of width 0.25 dex, we obtain the median metallicity and the offset of each galaxy from that median. We plot this offset as a function of sSFR and denote the slope of this relation  $\eta_{\text{SFR}}$ . Figure 5 then depicts the  $\eta_{\text{SFR}}$  values for all nine metallicity diagnostics for each mass bin. The  $\eta_{\text{SFR}}$  values follow the same trend: positive for the lowest mass bin(s), negative for  $10^{8.5}M_\odot < M < 10^{10.5}M_\odot$ , and then inverting to positive at masses greater than  $10^{10.5}M_\odot$ . We therefore conclude that the choice of metallicity diagnostic in our analysis does not systematically affect our results.

#### 4.3. Expanding to redshift $0 < z < 1$

To generalize our results, we performed the same analysis described in Sections 3.2 and 4.1, using data not just from redshift  $z = 0$ , but also for different increments up to redshift  $z = 1$ . Figure 6 shows  $\eta_{\text{SFR}}$  values for the four simulations we use at redshifts  $z = 0, 0.1, 0.3, 0.5, 0.7$ , and  $1.0$ .

For three simulations (Illustris, TNG, and EAGLE), the behavior established in Section 3.2 at  $z = 0$  remains visible at higher redshifts: negative  $\eta_{\text{SFR}}$  values for mass bins up to  $10^{10.5}M_\odot$  with an inversion to positive  $\eta_{\text{SFR}}$  in the highest mass bins. Figure 6 was created using the fiducial threshold of  $T = -0.5$  dex, however the patterns established in Section 4.1 for  $T = -0.1$  dex and  $-\infty$  dex (negative  $\eta_{\text{SFR}}$  values at all mass bins and an inversion

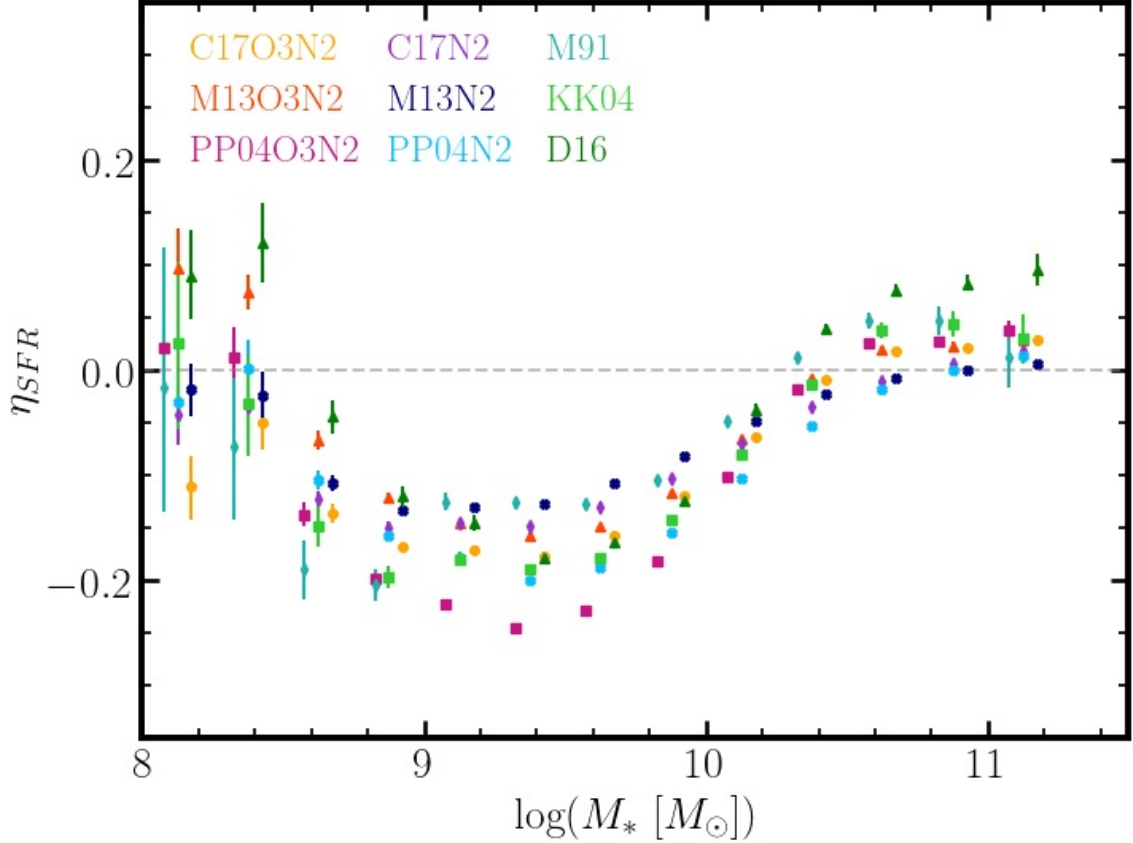


**Figure 5.** Comparison of  $\eta_{\text{SFR}}$  values as a function of mass for mass bins of width 0.25 dex using  $T = -0.5$  and at  $z = 0$  for different SDSS metallicity diagnostics.

around  $10^{10}M_\odot$ , respectively) also hold for redshifts up to  $z = 1$ .

For redshifts  $z = 0.1$ , and  $0.3$ , SIMBA behaves the same as for  $z = 0$ . However, at redshifts  $\geq 0.5$ , there appears an inversion in the opposite direction, with positive  $\eta_{\text{SFR}}$  values at masses below  $10^{10}M_\odot$  and negative  $\eta_{\text{SFR}}$  values above  $10^{10}M_\odot$ . One possible reason for this is the change in the mass loading factor with redshift: the mass loading is suppressed by a factor of  $a/0.25$  (where  $a \equiv 1/[1+z]$ ) (Davé et al. 2019). At redshift  $z = 0$ , this factor is equal to 4, at  $z = 1$ , it is equal to 2.  $z = 1$  galaxies are suppressed less heavily, which combined with strong winds at lower masses can lead to positive  $\eta_{\text{SFR}}$  values for low-mass galaxies, but negative  $\eta_{\text{SFR}}$  for high-mass galaxies with less blowout. The change in this behavior in the  $10^{9.75}M_\odot$  mass bin is therefore likely due to the mass loading factors themselves changing behavior at a mass of  $M = 10^{9.7}M_\odot$ .

#### 4.4. Physical Process

The physical process suggested in the standard, invariant FMR is the one that has already been discussed in this paper. A galaxy accretes gas, lowering its metallicity, which fuels the birth of new stars, increasing its

SFR. As this gas is being used up, the SFR decreases, and as the stars die, they release metals into the galactic environment, raising the metallicity. A schematic model of this “standard FMR mode” is depicted in the left panel of Figure 7. This process results in negative  $\eta_{\text{SFR}}$  values like those in the insets of Figure 2 — high SFRs are correlated with low metallicities and low SFRs are correlated with high metallicities (i.e., a negative correlation).

This physical picture could equally be used to explain the process resulting in the negative  $\eta_{\text{SFR}}$  values at lower mass bins in Figure 3. However, it does not explain the inversion to positive  $\eta_{\text{SFR}}$  values at higher mass bins. We propose the following physical mechanism, in which galaxies with larger masses experience quenching (lower sSFR) at the same time as metals are ejected (lower metallicity), which leads to a positive correlation between the two quantities, i.e. a positive  $\eta_{\text{SFR}}$  value: Galaxies with larger masses tend to have AGN, which produce outflows (McAlpine et al. 2017; Weinberger et al. 2017; Torrey et al. 2019; Wright et al. 2024). Specifically, Torrey et al. (2019), looking at how galaxies in the TNG simulation move from redshift  $z = 0.058$

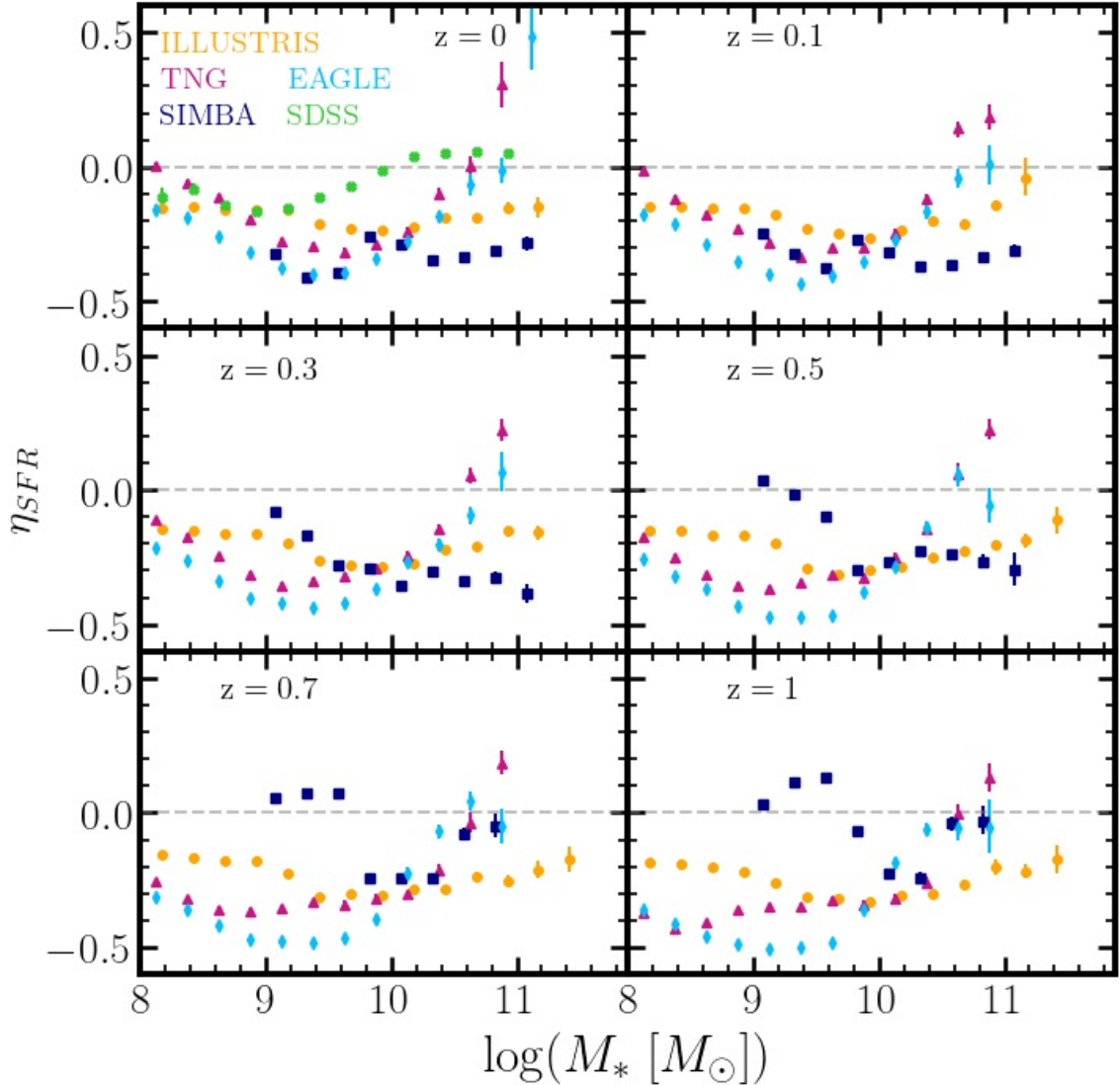


**Figure 6.** Comparison of  $\eta_{\text{SFR}}$  as a function of mass for mass bins of width 0.25 dex using  $T = -0.5$  for each of the four simulations (Illustris, TNG, SIMBA, EAGLE) and SDSS at 6 different redshifts:  $z = 0$  (top left, equivalent to Fig. 3),  $z = 0.1$  (top right),  $z = 0.3$  (middle left),  $z = 0.5$  (middle right),  $z = 0.7$  (bottom left), and  $z = 1$  (bottom right). Note that SDSS data is only included for  $z = 0$ .

to  $z = 0$ , have shown that at masses  $> 10^{10.5} M_{\odot}$ , the galaxies go from being accretion- (increasing ISM mass, decreasing metallicity) or enrichment-dominated (decreasing ISM mass, increasing metallicity) to being outflow-dominated (decreasing ISM mass, constant metallicity; see Figure 13 in Torrey et al. 2019). Higher mass galaxies in this case lose ISM mass while maintaining a constant metallicity, meaning they lose both hydrogen and metals to the outflows. Similarly, Wright et al. (2024) show that in TNG, EAGLE, and SIMBA, AGN-driven outflows are expelled to approximately  $R_{200c}$  (the radius at which the density becomes  $200 \times \rho_{\text{critical}}$ ) or further. However, in these simulations, quantities like gas-phase metallicity are measured over a radius of around

$2R_{\star}$  ( $\sim 30$  kpc), which is significantly smaller than  $R_{200c}$ . The AGN, being located in the center of their galaxy, preferentially blow out material located nearby, i.e. material located in the center of the galaxy, which tends to be more metal-enriched than the outskirts (e.g., Garcia et al. 2025b). Given this, we suspect that AGN in high-mass galaxies cause the ejection of metals to a point where they are no longer factored in to the metallicity calculation, leading to a decrease in metallicity. At the same time, the presence of these AGN causes galaxies to quench, decreasing the sSFR.

De Rossi et al. (2017) have used the EAGLE simulation to investigate the effect of AGN on the MZR and FMR. They found that the AGN feedback starts to have



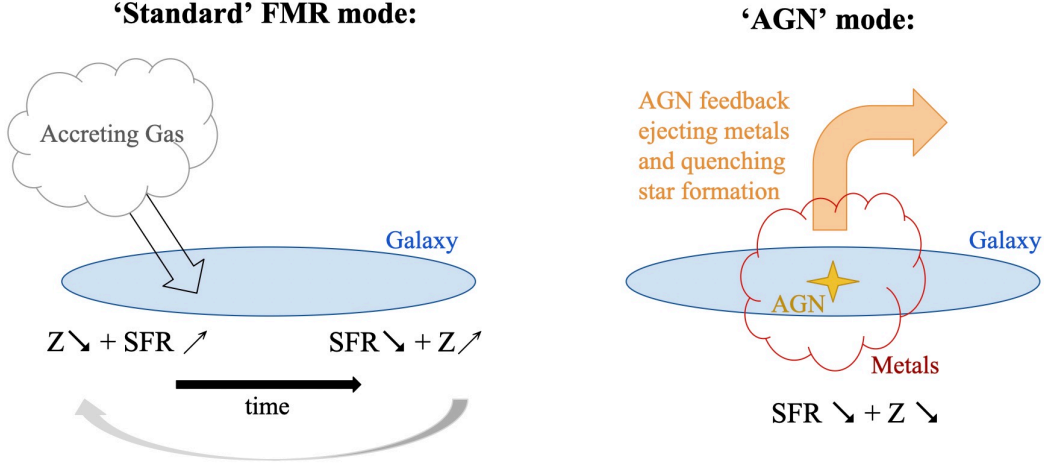


**Figure 7.** Simplified models of the physical processes involved in the ‘standard’ and proposed AGN modes. *Left:* ‘Standard’ FMR model, wherein as gas is accreted, the metallicity decreases and SFR increases. Once the gas is used up and stars die and release metals, the SFR decreases and the metallicity increases. *Right:* Proposed AGN mode, showing a higher concentration of metals near the center of a galaxy, where they are preferentially blown out by AGN feedback, resulting in metallicity and SFR decreasing at the same time (inversion).

an influence at masses  $> 10^{10.5} M_{\odot}$ , the same threshold point where the inversion of  $\eta_{\text{SFR}}$  in our results occurs. In the lowest panel of their Figure 3, they show that if no AGN is present, the metallicity continues to increase with stellar mass. However, if an AGN is present, the metallicity plateaus or decreases at masses  $> 10^{10.5} M_{\odot}$ , as metals are ejected from the galactic environment. De Rossi et al. show that the presence of AGN (feedback) has an influence on the behavior of the MZR/FMR via the AGN’s effect on the metallicity evolution.

This, in effect, is what we are suggesting is occurring here across our data sources. The inversion of  $\eta_{\text{SFR}}$  values occurs at a mass between  $10^{10}$  and  $10^{11} M_{\odot}$  — the threshold where galaxies begin to be outflow-dominated and AGN feedback has more of an influence (Torrey et al. 2019; De Rossi et al. 2017). We propose that at higher masses, the presence of AGN causes outflows of mainly metal-enriched material, as that is more concentrated in the center of the galaxy (Garcia et al. 2025b), which are ejected far enough to no longer be counted when calculation the galaxy’s metallicity (Wright et al. 2024). At the same time, the presence of the AGN causes quenching, i.e. a decrease in sSFR. This simultaneous decrease in metallicity and sSFR at masses  $> 10^{10.5} M_{\odot}$  then leads to positive  $\eta_{\text{SFR}}$  values. A simplified depiction of this mechanism (‘AGN’ mode) can be found on the right panel of Figure 7. Our analysis in Section 4.1 and Figure 4 lends further support to this suggestion (at least, for the simulations): increasing the sSFR of the galaxies we select leads to a decrease

in inversion, while selecting galaxies with lower sSFRs increases the presence of the inversion, tying the presence/strength of the inversion to the sSFR of the galaxies, potentially further linking the inversion to AGN.

To briefly address the positive  $\eta_{\text{SFR}}$  values at the lowest mass bins for some of our data sources: One possible explanation is that low-mass galaxies have lower gravitational potentials, which can make it more likely for them to ‘lose’ their metals than higher mass galaxies, leading to a lower metallicity. Further, this turnover of  $\eta_{\text{SFR}}$  is present to a greater extent as more galaxies with low sSFRs are included. This decrease in sSFR at lower masses is not caused by AGN feedback as we suggest for high-mass galaxies, but could be caused by events such as galaxy mergers or even strong supernova feedback. This is a possible scenario in which we can have a simultaneous decrease in metallicity and SFR in low-mass galaxies, which would result in the positive  $\eta_{\text{SFR}}$  values observed in Figure 4.

## 5. CONCLUSIONS

In this paper, we investigate the mass dependence of the residual correlation with sSFR about the MZR using data from the cosmological simulations EAGLE, SIMBA, Illustris, and TNG, as well as from SDSS observations. In doing our analysis, we restrict the galaxies we use to those that present a minimum threshold of star formation and vary this threshold to study the effect of low-sSFR galaxies on our results. We also expand our

analysis from redshift  $z = 0$  in increments up to  $z = 1$ . We reach the following conclusions:

- We find that there is an anti-correlation between offsets from the MZR based on sSFR at  $z = 0$ , with lower metallicities corresponding to higher sSFRs, and vice-versa (Figure 2). We quantify this anti-correlation by defining  $\eta_{\text{SFR}}$  as the slope of the relation between  $\Delta Z$  and sSFR (Equation 1). We find that the  $\eta_{\text{SFR}}$  is negative in all four simulations and our SDSS sample when considering all galaxies (insets of Figure 2).
- We find that, when considering  $\eta_{\text{SFR}}$  broken into thin stellar mass bins, there is an inversion of  $\eta_{\text{SFR}}$  at higher masses ( $M_{\star} > 10^{10.5} M_{\odot}$ ) for SDSS, TNG, and EAGLE (Figure 3).
- We show that adjusting our galaxy selection criteria by changing the SFR threshold from its fiducial value of  $T = -0.5$  dex below the sSFR main sequence has an effect on the inversion of  $\eta_{\text{SFR}}$  (Figure 4). Restricting our sample to include fewer low-sSFR galaxies ( $T = -0.1$  dex) reduces the inversion, whereas relaxing the threshold to include more low-sSFR galaxies ( $T = -1, -\infty$  dex) makes the inversion more pronounced. Using  $T = -\infty$  dex, the inversion of  $\eta_{\text{SFR}}$  is present for all five data sources at the highest masses. We conclude that the inversion is related to, and caused by, the presence of low sSFR galaxies in our analysis.
- We find that our results are independent of the choice of SDSS metallicity diagnostic (Figure 5), suggesting that our observational results are robust to uncertainties in metallicity calibration.
- We find that the established trend (inversion of  $\eta_{\text{SFR}}$  values at higher masses) remains present at redshifts up to  $z = 1$  (Figure 6).
- We propose an alternative physical picture to the ‘standard’ model used to explain the anti-correlation of metallicity and sSFR, which would account for the resulting positive correlation between SFR and metallicity of high-mass galaxies

(Figure 7). Specifically, we suggest that AGN feedback, which is most dominant in high-mass galaxies, simultaneously quenches star formation (lowering the SFR) and preferentially blows out metals, which are concentrated in the center of the galaxy (lowering the metallicity), leading to a positive value for  $\eta_{\text{SFR}}$ .

We have shown that there exists a residual correlation about the MZR that changes its behavior at higher masses ( $M > 10^{10.5} M_{\odot}$ ) across simulations (Illustris, TNG, EAGLE, SIMBA) and observations (SDSS data) up to at least  $z = 1$ . The ubiquity of the (anti-)correlations of metallicity and SFR in all our models and observations gives hints towards a larger picture of galactic scale physics. Yet, treating these subtle processes with a single mass and redshift invariant relationship glosses over critical pieces of physics. Having a clearly quantified way to measure the anti-correlation between metallicity and sSFR as a function of mass allows for a more robust understanding of the story metals and SFR tell us. This framework allows us to more fully see the connection of the inversion to the inclusion of low sSFR galaxies, which in turn allows for a new physical description of this relation in high-mass galaxies. It also provides a means of understanding mechanisms that quench galaxies. This can put future constraints on implementing structures that influence the behavior of metallicity in simulations, like AGN feedback or mass loading factors, which would not be possible by treating the FMR in a rigid framework.

The authors acknowledge Research Computing at The University of Virginia for providing computational resources and technical support that have contributed to the results reported within this publication. URL: <https://rc.virginia.edu>.

AMG and PT acknowledge support from NSF-AST 2346977 and the NSF-Simons AI Institute for Cosmic Origins which is supported by the National Science Foundation under Cooperative Agreement 2421782 and the Simons Foundation award MPS-AI-00010515.

KG is supported by the Australian Research Council through the Discovery Early Career Researcher Award (DECRA) Fellowship (project number DE220100766) funded by the Australian Government.

## REFERENCES

- Abazajian, K. N., Adelman-McCarthy, J. K., Agüeros, M. A., et al. 2009, *ApJS*, 182, 543, doi: [10.1088/0067-0049/182/2/543](https://doi.org/10.1088/0067-0049/182/2/543)
- Anglés-Alcázar, D., Davé, R., Faucher-Giguère, C.-A., Özel, F., & Hopkins, P. F. 2017a, *MNRAS*, 464, 2840, doi: [10.1093/mnras/stw2565](https://doi.org/10.1093/mnras/stw2565)

- Anglés-Alcázar, D., Faucher-Giguère, C.-A., Kereš, D., et al. 2017b, *MNRAS*, 470, 4698, doi: [10.1093/mnras/stx1517](https://doi.org/10.1093/mnras/stx1517)
- Baker, W. M., & Maiolino, R. 2023, *MNRAS*, 521, 4173, doi: [10.1093/mnras/stad802](https://doi.org/10.1093/mnras/stad802)
- Baldwin, J. A., Phillips, M. M., & Terlevich, R. 1981, *PASP*, 93, 5, doi: [10.1086/130766](https://doi.org/10.1086/130766)
- Bassini, L., Feldmann, R., Gensior, J., et al. 2024, *MNRAS*, 532, L14, doi: [10.1093/mnrasl/slae036](https://doi.org/10.1093/mnrasl/slae036)
- Bondi, H. 1952, *MNRAS*, 112, 195, doi: [10.1093/mnras/112.2.195](https://doi.org/10.1093/mnras/112.2.195)
- Bothwell, M. S., Maiolino, R., Kennicutt, R., et al. 2013, *MNRAS*, 433, 1425, doi: [10.1093/mnras/stt817](https://doi.org/10.1093/mnras/stt817)
- Bothwell, M. S., Maiolino, R., Peng, Y., et al. 2016, *MNRAS*, 455, 1156, doi: [10.1093/mnras/stv2121](https://doi.org/10.1093/mnras/stv2121)
- Brinchmann, J., Charlot, S., Heckman, T. M., et al. 2004, arXiv e-prints, astro, doi: [10.48550/arXiv.astro-ph/0406220](https://doi.org/10.48550/arXiv.astro-ph/0406220)
- Crain, R. A., Schaye, J., Bower, R. G., et al. 2015, *MNRAS*, 450, 1937, doi: [10.1093/mnras/stv725](https://doi.org/10.1093/mnras/stv725)
- Curti, M., Cresci, G., Mannucci, F., et al. 2017, *MNRAS*, 465, 1384, doi: [10.1093/mnras/stw2766](https://doi.org/10.1093/mnras/stw2766)
- Curti, M., Maiolino, R., Curtis-Lake, E., et al. 2024, *A&A*, 684, A75, doi: [10.1051/0004-6361/202346698](https://doi.org/10.1051/0004-6361/202346698)
- Dalla Vecchia, C., & Schaye, J. 2012, *MNRAS*, 426, 140, doi: [10.1111/j.1365-2966.2012.21704.x](https://doi.org/10.1111/j.1365-2966.2012.21704.x)
- Davé, R., Anglés-Alcázar, D., Narayanan, D., et al. 2019, *MNRAS*, 486, 2827, doi: [10.1093/mnras/stz937](https://doi.org/10.1093/mnras/stz937)
- Davé, R., Finlator, K., & Oppenheimer, B. D. 2011, *MNRAS*, 416, 1354, doi: [10.1111/j.1365-2966.2011.19132.x](https://doi.org/10.1111/j.1365-2966.2011.19132.x)
- Davé, R., Thompson, R., & Hopkins, P. F. 2016, *MNRAS*, 462, 3265, doi: [10.1093/mnras/stw1862](https://doi.org/10.1093/mnras/stw1862)
- De Rossi, M. E., Bower, R. G., Font, A. S., Schaye, J., & Theuns, T. 2017, *MNRAS*, 472, 3354, doi: [10.1093/mnras/stx2158](https://doi.org/10.1093/mnras/stx2158)
- De Rossi, M. E., Theuns, T., Font, A. S., & McCarthy, I. G. 2015, *MNRAS*, 452, 486, doi: [10.1093/mnras/stv1287](https://doi.org/10.1093/mnras/stv1287)
- Dekel, A., & Birnboim, Y. 2006, *MNRAS*, 368, 2, doi: [10.1111/j.1365-2966.2006.10145.x](https://doi.org/10.1111/j.1365-2966.2006.10145.x)
- Dopita, M. A., Kewley, L. J., Sutherland, R. S., & Nicholls, D. C. 2016, *Ap&SS*, 361, 61, doi: [10.1007/s10509-016-2657-8](https://doi.org/10.1007/s10509-016-2657-8)
- Ellison, S. L., Patton, D. R., Simard, L., & McConnachie, A. W. 2008, *AJ*, 135, 1877, doi: [10.1088/0004-6256/135/5/1877](https://doi.org/10.1088/0004-6256/135/5/1877)
- Fishlock, C. K., Karakas, A. I., Lugaro, M., & Yong, D. 2014, *ApJ*, 797, 44, doi: [10.1088/0004-637X/797/1/44](https://doi.org/10.1088/0004-637X/797/1/44)
- Friedli, D., Benz, W., & Kennicutt, R. 1994, *ApJL*, 430, L105, doi: [10.1086/187449](https://doi.org/10.1086/187449)
- Garcia, A. M., Torrey, P., Hemler, Z. S., et al. 2023, *MNRAS*, 519, 4716, doi: [10.1093/mnras/stac3749](https://doi.org/10.1093/mnras/stac3749)
- Garcia, A. M., Torrey, P., Ellison, S., et al. 2024a, *MNRAS*, 531, 1398, doi: [10.1093/mnras/stae1252](https://doi.org/10.1093/mnras/stae1252)
- Garcia, A. M., Torrey, P., Grasha, K., et al. 2024b, *MNRAS*, 529, 3342, doi: [10.1093/mnras/stae737](https://doi.org/10.1093/mnras/stae737)
- Garcia, A. M., Torrey, P., Ellison, S. L., et al. 2025a, *MNRAS*, 536, 119, doi: [10.1093/mnras/stae2587](https://doi.org/10.1093/mnras/stae2587)
- Garcia, A. M., Torrey, P., Bhagwat, A., et al. 2025b, arXiv e-prints, arXiv:2503.03804, doi: [10.48550/arXiv.2503.03804](https://doi.org/10.48550/arXiv.2503.03804)
- Genel, S., Vogelsberger, M., Springel, V., et al. 2014, *MNRAS*, 445, 175, doi: [10.1093/mnras/stu1654](https://doi.org/10.1093/mnras/stu1654)
- Gunn, J. E., Siegmund, W. A., Mannery, E. J., et al. 2006, *AJ*, 131, 2332, doi: [10.1086/500975](https://doi.org/10.1086/500975)
- Hemler, Z. S., Torrey, P., Qi, J., et al. 2021, *MNRAS*, 506, 3024, doi: [10.1093/mnras/stab1803](https://doi.org/10.1093/mnras/stab1803)
- Hinshaw, G., Larson, D., Komatsu, E., et al. 2013, *ApJS*, 208, 19, doi: [10.1088/0067-0049/208/2/19](https://doi.org/10.1088/0067-0049/208/2/19)
- Hogg, D. W., Blanton, M., & SDSS Collaboration. 2001, in American Astronomical Society Meeting Abstracts, Vol. 199, American Astronomical Society Meeting Abstracts, 160.07
- Hopkins, P. F. 2015, *MNRAS*, 450, 53, doi: [10.1093/mnras/stv195](https://doi.org/10.1093/mnras/stv195)
- . 2017, arXiv e-prints, arXiv:1712.01294, doi: [10.48550/arXiv.1712.01294](https://doi.org/10.48550/arXiv.1712.01294)
- Hopkins, P. F., & Quataert, E. 2011, *MNRAS*, 415, 1027, doi: [10.1111/j.1365-2966.2011.18542.x](https://doi.org/10.1111/j.1365-2966.2011.18542.x)
- Iwamoto, K., Brachwitz, F., Nomoto, K., et al. 1999, *ApJS*, 125, 439, doi: [10.1086/313278](https://doi.org/10.1086/313278)
- Jain, S., Sanders, R. L., Khostovan, A. A., et al. 2025, arXiv e-prints, arXiv:2508.18369, <https://arxiv.org/abs/2508.18369>
- Karakas, A. I. 2010, *MNRAS*, 403, 1413, doi: [10.1111/j.1365-2966.2009.16198.x](https://doi.org/10.1111/j.1365-2966.2009.16198.x)
- Kauffmann, G., Heckman, T. M., White, S. D. M., et al. 2003, *MNRAS*, 341, 33, doi: [10.1046/j.1365-8711.2003.06291.x](https://doi.org/10.1046/j.1365-8711.2003.06291.x)
- Kennicutt, R. C., & Evans, N. J. 2012, *ARA&A*, 50, 531, doi: [10.1146/annurev-astro-081811-125610](https://doi.org/10.1146/annurev-astro-081811-125610)
- Kennicutt, Jr., R. C. 1998, *ApJ*, 498, 541, doi: [10.1086/305588](https://doi.org/10.1086/305588)
- Kereš, D., Katz, N., Weinberg, D. H., & Davé, R. 2005, *MNRAS*, 363, 2, doi: [10.1111/j.1365-2966.2005.09451.x](https://doi.org/10.1111/j.1365-2966.2005.09451.x)
- Kobayashi, C., Umeda, H., Nomoto, K., Tominaga, N., & Ohkubo, T. 2006, *ApJ*, 653, 1145, doi: [10.1086/508914](https://doi.org/10.1086/508914)
- Kobulnicky, H. A., & Kewley, L. J. 2004, *ApJ*, 617, 240, doi: [10.1086/425299](https://doi.org/10.1086/425299)
- Koeppen, J. 1994, *A&A*, 281, 26

- Krumholz, M. R., & Gnedin, N. Y. 2011, *ApJ*, 729, 36, doi: [10.1088/0004-637X/729/1/36](https://doi.org/10.1088/0004-637X/729/1/36)
- Lacey, C. G., & Fall, S. M. 1985, *ApJ*, 290, 154, doi: [10.1086/162970](https://doi.org/10.1086/162970)
- Lagos, C. d. P., Valentino, F., Wright, R. J., et al. 2025, *MNRAS*, 536, 2324, doi: [10.1093/mnras/stae2626](https://doi.org/10.1093/mnras/stae2626)
- Lara-López, M. A., Cepa, J., Bongiovanni, A., et al. 2010, *A&A*, 521, L53, doi: [10.1051/0004-6361/201014803](https://doi.org/10.1051/0004-6361/201014803)
- Lequeux, J., Peimbert, M., Rayo, J. F., Serrano, A., & Torres-Peimbert, S. 1979, *A&A*, 80, 155
- Li, M., Cai, Z., Bian, F., et al. 2023, *ApJL*, 955, L18, doi: [10.3847/2041-8213/acf470](https://doi.org/10.3847/2041-8213/acf470)
- Ma, C., Wang, K., Wang, E., et al. 2024, *ApJL*, 971, L14, doi: [10.3847/2041-8213/ad675f](https://doi.org/10.3847/2041-8213/ad675f)
- Mannucci, F., Cresci, G., Maiolino, R., Marconi, A., & Gnerucci, A. 2010, *MNRAS*, 408, 2115, doi: [10.1111/j.1365-2966.2010.17291.x](https://doi.org/10.1111/j.1365-2966.2010.17291.x)
- Marigo, P. 2001, *A&A*, 370, 194, doi: [10.1051/0004-6361:20000247](https://doi.org/10.1051/0004-6361:20000247)
- Marinacci, F., Vogelsberger, M., Pakmor, R., et al. 2018, *MNRAS*, 480, 5113, doi: [10.1093/mnras/sty2206](https://doi.org/10.1093/mnras/sty2206)
- Marino, R. A., Rosales-Ortega, F. F., Sánchez, S. F., et al. 2013, *A&A*, 559, A114, doi: [10.1051/0004-6361/201321956](https://doi.org/10.1051/0004-6361/201321956)
- McAlpine, S., Bower, R. G., Harrison, C. M., et al. 2017, *MNRAS*, 468, 3395, doi: [10.1093/mnras/stx658](https://doi.org/10.1093/mnras/stx658)
- McGaugh, S. S. 1991, *ApJ*, 380, 140, doi: [10.1086/170569](https://doi.org/10.1086/170569)
- McKee, C. F., & Ostriker, E. C. 2007, *ARA&A*, 45, 565, doi: [10.1146/annurev.astro.45.051806.110602](https://doi.org/10.1146/annurev.astro.45.051806.110602)
- Muratov, A. L., Kereš, D., Faucher-Giguère, C.-A., et al. 2015, *MNRAS*, 454, 2691, doi: [10.1093/mnras/stv2126](https://doi.org/10.1093/mnras/stv2126)
- Naiman, J. P., Pillepich, A., Springel, V., et al. 2018, *MNRAS*, 477, 1206, doi: [10.1093/mnras/sty618](https://doi.org/10.1093/mnras/sty618)
- Nakajima, K., Ouchi, M., Isobe, Y., et al. 2023, *ApJS*, 269, 33, doi: [10.3847/1538-4365/acd556](https://doi.org/10.3847/1538-4365/acd556)
- Nelson, D., Pillepich, A., Springel, V., et al. 2018, *MNRAS*, 475, 624, doi: [10.1093/mnras/stx3040](https://doi.org/10.1093/mnras/stx3040)
- Nelson, D., Springel, V., Pillepich, A., et al. 2019a, *Computational Astrophysics and Cosmology*, 6, 2, doi: [10.1186/s40668-019-0028-x](https://doi.org/10.1186/s40668-019-0028-x)
- Nelson, D., Pillepich, A., Springel, V., et al. 2019b, *MNRAS*, 490, 3234, doi: [10.1093/mnras/stz2306](https://doi.org/10.1093/mnras/stz2306)
- Nomoto, K., Iwamoto, K., Nakasato, N., et al. 1997, *NuPhA*, 621, 467, doi: [10.1016/S0375-9474\(97\)00291-1](https://doi.org/10.1016/S0375-9474(97)00291-1)
- Nomoto, K., Tominaga, N., Umeda, H., Kobayashi, C., & Maeda, K. 2006, *NuPhA*, 777, 424, doi: [10.1016/j.nuclphysa.2006.05.008](https://doi.org/10.1016/j.nuclphysa.2006.05.008)
- Oppenheimer, B. D., & Davé, R. 2006, *MNRAS*, 373, 1265, doi: [10.1111/j.1365-2966.2006.10989.x](https://doi.org/10.1111/j.1365-2966.2006.10989.x)
- Pakmor, R., Bauer, A., & Springel, V. 2011, *MNRAS*, 418, 1392, doi: [10.1111/j.1365-2966.2011.19591.x](https://doi.org/10.1111/j.1365-2966.2011.19591.x)
- Pettini, M., & Pagel, B. E. J. 2004, *MNRAS*, 348, L59, doi: [10.1111/j.1365-2966.2004.07591.x](https://doi.org/10.1111/j.1365-2966.2004.07591.x)
- Pier, J. R., Munn, J. A., Hindsley, R. B., et al. 2003, *AJ*, 125, 1559, doi: [10.1086/346138](https://doi.org/10.1086/346138)
- Pillepich, A., Nelson, D., Hernquist, L., et al. 2018a, *MNRAS*, 475, 648, doi: [10.1093/mnras/stx3112](https://doi.org/10.1093/mnras/stx3112)
- Pillepich, A., Springel, V., Nelson, D., et al. 2018b, *MNRAS*, 473, 4077, doi: [10.1093/mnras/stx2656](https://doi.org/10.1093/mnras/stx2656)
- Pillepich, A., Nelson, D., Springel, V., et al. 2019, *MNRAS*, 490, 3196, doi: [10.1093/mnras/stz2338](https://doi.org/10.1093/mnras/stz2338)
- Pistis, F., Pollo, A., Figueira, M., et al. 2024, *A&A*, 683, A203, doi: [10.1051/0004-6361/202346943](https://doi.org/10.1051/0004-6361/202346943)
- Planck Collaboration, Ade, P. A. R., Aghanim, N., et al. 2014, *A&A*, 571, A16, doi: [10.1051/0004-6361/201321591](https://doi.org/10.1051/0004-6361/201321591)
- . 2016, *A&A*, 594, A13, doi: [10.1051/0004-6361/201525830](https://doi.org/10.1051/0004-6361/201525830)
- Portinari, L., Chiosi, C., & Bressan, A. 1998, *A&A*, 334, 505, doi: [10.48550/arXiv.astro-ph/9711337](https://doi.org/10.48550/arXiv.astro-ph/9711337)
- Salim, S., Rich, R. M., Charlot, S., et al. 2007, *ApJS*, 173, 267, doi: [10.1086/519218](https://doi.org/10.1086/519218)
- Sánchez-Menguiano, L., Sánchez, S. F., Sánchez Almeida, J., & Muñoz-Tuñón, C. 2024, *A&A*, 682, L11, doi: [10.1051/0004-6361/202348423](https://doi.org/10.1051/0004-6361/202348423)
- Sanders, R. L., Shapley, A. E., Kriek, M., et al. 2018, *ApJ*, 858, 99, doi: [10.3847/1538-4357/aabcbdb](https://doi.org/10.3847/1538-4357/aabcbdb)
- Sarkar, A., Chakraborty, P., Vogelsberger, M., et al. 2025, *ApJ*, 978, 136, doi: [10.3847/1538-4357/ad8f32](https://doi.org/10.3847/1538-4357/ad8f32)
- Savaglio, S., Glazebrook, K., Le Borgne, D., et al. 2005, *ApJ*, 635, 260, doi: [10.1086/497331](https://doi.org/10.1086/497331)
- Schaller, M., Dalla Vecchia, C., Schaye, J., et al. 2015, *MNRAS*, 454, 2277, doi: [10.1093/mnras/stv2169](https://doi.org/10.1093/mnras/stv2169)
- Schaye, J. 2004, *ApJ*, 609, 667, doi: [10.1086/421232](https://doi.org/10.1086/421232)
- Schaye, J., & Dalla Vecchia, C. 2008, *MNRAS*, 383, 1210, doi: [10.1111/j.1365-2966.2007.12639.x](https://doi.org/10.1111/j.1365-2966.2007.12639.x)
- Schaye, J., Crain, R. A., Bower, R. G., et al. 2015, *MNRAS*, 446, 521, doi: [10.1093/mnras/stu2058](https://doi.org/10.1093/mnras/stu2058)
- Segers, M. C., Crain, R. A., Schaye, J., et al. 2016, *MNRAS*, 456, 1235, doi: [10.1093/mnras/stv2562](https://doi.org/10.1093/mnras/stv2562)
- Sijacki, D., Vogelsberger, M., Genel, S., et al. 2015, *MNRAS*, 452, 575, doi: [10.1093/mnras/stv1340](https://doi.org/10.1093/mnras/stv1340)
- Springel, V. 2005, *MNRAS*, 364, 1105, doi: [10.1111/j.1365-2966.2005.09655.x](https://doi.org/10.1111/j.1365-2966.2005.09655.x)
- . 2010, *MNRAS*, 401, 791, doi: [10.1111/j.1365-2966.2009.15715.x](https://doi.org/10.1111/j.1365-2966.2009.15715.x)
- Springel, V., Di Matteo, T., & Hernquist, L. 2005, *MNRAS*, 361, 776, doi: [10.1111/j.1365-2966.2005.09238.x](https://doi.org/10.1111/j.1365-2966.2005.09238.x)
- Springel, V., & Hernquist, L. 2003, *MNRAS*, 339, 289, doi: [10.1046/j.1365-8711.2003.06206.x](https://doi.org/10.1046/j.1365-8711.2003.06206.x)



- Springel, V., Pakmor, R., Pillepich, A., et al. 2018, MNRAS, 475, 676, doi: [10.1093/mnras/stx3304](https://doi.org/10.1093/mnras/stx3304)
- Stephenson, H. M. O., Stott, J. P., Cullen, F., et al. 2024, MNRAS, 527, 7891, doi: [10.1093/mnras/stad3721](https://doi.org/10.1093/mnras/stad3721)
- Thielemann, F. K., Argast, D., Brachwitz, F., et al. 2003, NuPhA, 718, 139, doi: [10.1016/S0375-9474\(03\)00704-8](https://doi.org/10.1016/S0375-9474(03)00704-8)
- Torrey, P., Vogelsberger, M., Genel, S., et al. 2014, MNRAS, 438, 1985, doi: [10.1093/mnras/stt2295](https://doi.org/10.1093/mnras/stt2295)
- Torrey, P., Vogelsberger, M., Hernquist, L., et al. 2018, MNRAS, 477, L16, doi: [10.1093/mnrasl/sly031](https://doi.org/10.1093/mnrasl/sly031)
- Torrey, P., Vogelsberger, M., Marinacci, F., et al. 2019, MNRAS, 484, 5587, doi: [10.1093/mnras/stz243](https://doi.org/10.1093/mnras/stz243)
- Tremonti, C. A., Heckman, T. M., Kauffmann, G., et al. 2004, ApJ, 613, 898, doi: [10.1086/423264](https://doi.org/10.1086/423264)
- Vogelsberger, M., Genel, S., Sijacki, D., et al. 2013, MNRAS, 436, 3031, doi: [10.1093/mnras/stt1789](https://doi.org/10.1093/mnras/stt1789)
- Vogelsberger, M., Genel, S., Springel, V., et al. 2014a, MNRAS, 444, 1518, doi: [10.1093/mnras/stu1536](https://doi.org/10.1093/mnras/stu1536)
- . 2014b, Nature, 509, 177, doi: [10.1038/nature13316](https://doi.org/10.1038/nature13316)
- Weinberger, R., Springel, V., Hernquist, L., et al. 2017, MNRAS, 465, 3291, doi: [10.1093/mnras/stw2944](https://doi.org/10.1093/mnras/stw2944)
- Weinberger, R., Springel, V., Pakmor, R., et al. 2018, MNRAS, 479, 4056, doi: [10.1093/mnras/sty1733](https://doi.org/10.1093/mnras/sty1733)
- Wright, R. J., Somerville, R. S., Lagos, C. d. P., et al. 2024, MNRAS, 532, 3417, doi: [10.1093/mnras/stae1688](https://doi.org/10.1093/mnras/stae1688)
- Yates, R. M., Kauffmann, G., & Guo, Q. 2012, MNRAS, 422, 215, doi: [10.1111/j.1365-2966.2012.20595.x](https://doi.org/10.1111/j.1365-2966.2012.20595.x)
- Zahid, H. J., Kashino, D., Silverman, J. D., et al. 2014, ApJ, 792, 75, doi: [10.1088/0004-637X/792/1/75](https://doi.org/10.1088/0004-637X/792/1/75)